Research Article | Vol. 26, No. 8 | 16 Apr 2018 | OPTICS EXPRESS 10242

Optics EXPRESS

Point-cloud noncontact metrology of freeform optical surfaces

JIANING YAO,* ALEXANDER ANDERSON, AND JANNICK P. ROLLAND

The Institute of Optics, University of Rochester, Rochester, NY 14627, USA
**jyao@optics.rochester.edu*

Abstract: In this paper, we demonstrate the development of a point-cloud metrology method for the noncontact, high resolution, high precision testing of freeform surfaces. The method leverages swept source optical coherence tomography together with a common-path setup in the sample arm configured to mitigate the axial jitter caused by scanning and environmental perturbations. The lateral x-y scanning field was also rigorously evaluated for the sampling step, linearity, straightness, and orthogonality. Based on the finely engineered system hardware, a comprehensive system model was developed capable of characterizing the vertical displacement sensitivity and lateral scanning noise. The model enables predicting the point-cloud surface-metrology uncertainty map of any freeform surface and guiding the selection of optimum experimental conditions. A system was then assembled and experimentally evaluated first with flat and spherical standards to demonstrate the measurement uncertainty. Results of measuring an Alvarez freeform surface with 400-μm peak-to-valley sag show 93 nm (< λ/14) precision and 128 nm (< λ/10) root-mean-square residual from the nominal shape. The high resolution measurements also reveal mid spatial frequency structures on the test part.

OCIS codes: (120.0120) Instrumentation, measurement, and metrology; (110.4500) Optical coherence tomography; (080.4228) Nonspherical mirror surfaces.

References and links

1. K. P. Thompson and J. P. Rolland, "A revolution in imaging optical design," Opt. Photonics News **23**(6), 30–35 (2012).
2. K. Fuerschbach, J. P. Rolland, and K. P. Thompson, "A new family of optical systems employing φ-polynomial surfaces," Opt. Express **19**(22), 21919–21928 (2011).
3. J. McGuire, "A fast, wide-field of view, freeform TMA: design and tolerance analysis," in Imaging and Applied Optics 2015, OSA Technical Digest (online) (Optical Society of America, 2015), paper FW3B.4.
4. M. Chrisp, "Wide angle reflective telescopes with NURBS freeform surfaces," in Optical Design and Fabrication 2017 (Freeform, IODC, OFT), OSA Technical Digest (online) (Optical Society of America, 2017), paper JTu3A.2.
5. J. Reimers, A. Bauer, K. P. Thompson, and J. P. Rolland, "Freeform spectrometer enabling increased compactness," Light Sci. Appl. **6**(7), e17026 (2017).
6. A. Bauer and J. P. Rolland, "Visual space assessment of two all-reflective, freeform, optical see-through head-worn displays," Opt. Express **22**(11), 13155–13163 (2014).
7. D. Cheng, Y. Wang, C. Xu, W. Song, and G. Jin, "Design of an ultra-thin near-eye display with geometrical waveguide and freeform optics," Opt. Express **22**(17), 20705–20719 (2014).
8. S. Wills, "Freeform optics: notes from the revolution," Opt. Photonics News **28**(7), 34–41 (2017).
9. E. Savio, L. De Chiffre, and R. Schmitt, "Metrology of freeform shaped parts," CIRP Annals - Manufacturing Technology **56**(2), 810–835 (2007).
10. H. Takeuchi, K. Yosizumi, and H. Tsutsumi, "Ultrahigh accurate 3-D profilometer using atomic force probe of measuring nanometer," Proc. ASPE Winter Topical Meeting on Free-form optics: Design, Fabrication, Metrology and Assembly, 102–107 (2004).
11. A. Offner, "A null corrector for paraboloidal mirrors," Appl. Opt. **2**(2), 153–156 (1963).
12. K. Fuerschbach, K. P. Thompson, and J. P. Rolland, "Interferometric measurement of a concave, φ-polynomial, Zernike mirror," Opt. Lett. **39**(1), 18–21 (2014).
13. Y. M. Liu, G. N. Lawrence, and C. L. Koliopoulos, "Subaperture testing of aspheres with annular zones," Appl. Opt. **27**(21), 4504–4513 (1988).
14. P. Murphy, G. Forbes, J. Fleig, P. Dumas, and M. Tricard, "Stitching interferometry: a flexible solution for surface metrology," Opt. Photonics News **14**(5), 38–43 (2003).

#309511 https://doi.org/10.1364/OE.26.010242
Journal © 2018 Received 29 Dec 2017; revised 16 Mar 2018; accepted 19 Mar 2018; published 9 Apr 2018

Optics EXPRESS

15. S. Chen, S. Li, and Y. Dai, "Iterative algorithm for subaperture stitching interferometry for general surfaces," J. Opt. Soc. Am. A **22**(9), 1929–1936 (2005).
16. I. Kaya and J. P. Rolland, "Hybrid RBF and local ϕ-polynomial freeform surfaces," Adv. Opt. Technol. **2**(1), 81–88 (2013).
17. Y. S. Ghim, H. G. Rhee, A. Davies, H. S. Yang, and Y. W. Lee, "3D surface mapping of freeform optics using wavelength scanning lateral shearing interferometry," Opt. Express **22**(5), 5098–5105 (2014).
18. Q. Hao, S. Wang, Y. Hu, H. Cheng, M. Chen, and T. Li, "Virtual interferometer calibration method of a non-null interferometer for freeform surface measurements," Appl. Opt. **55**(35), 9992–10001 (2016).
19. G. Baer, J. Schindler, C. Pruss, J. Siepmann, and W. Osten, "Calibration of a non-null test interferometer for the measurement of aspheres and free-form surfaces," Opt. Express **22**(25), 31200–31211 (2014).
20. M. C. Knauer, J. Kaminski, and G. Hausler, "Phase measuring deflectometry: a new approach to measure specular free-form surfaces," Proc. SPIE **5457**, 366 (2004).
21. P. Su, R. E. Parks, L. Wang, R. P. Angel, and J. H. Burge, "Software configurable optical test system: a computerized reverse Hartmann test," Appl. Opt. **49**(23), 4404–4412 (2010).
22. D. Perard and J. Beyerer, "Three-dimensional measurement of specular free-form surfaces with a structured-lighting reflection technique," Proc. SPIE **3204**, 74–80 (1997).
23. T. Bothe, W. Li, C. von Kopylow, W. P. O. Juptner, "High-resolution 3D shape measurement on specular surfaces by fringe reflection," Proc. SPIE **5457**, 411 (2004).
24. C. Faber, E. Olesch, R. Krobot, and G. Häusler, "Deflectometry challenges interferometry – the competition gets tougher!" Proc. SPIE **8493**, 84930R (2012).
25. M. A. Browne, O. Akinyemi, and A. Boyde, "Confocal surface profiling utilizing chromatic aberration," Scanning **14**(3), 145–153 (1992).
26. D. Malacara, ed., *Optical Shop Testing*, 3rd ed. (John Wiley and Sons, 2007).
27. K. Falaggis, D. P. Towers, and C. E. Towers, "Multiwavelength interferometry: extended range metrology," Opt. Lett. **34**(7), 950–952 (2009).
28. J. Petter, "Multi wavelength interferometry for high precision distance measurement," in OPTO 2009 Proceedings of SENSOR + TEST Conference (2009), pp. 129–132.
29. A. Beutler, "Referencing and form measurements of freeform optics," in Optical Design and Fabrication 2017 (Freeform, IODC, OFT), OSA Technical Digest (online) (Optical Society of America, 2017), paper JTh1C.4.
30. S. Defisher, "Metrology for manufacturing of freeform optical surfaces with UltraSurf," in Imaging and Applied Optics 2015, OSA Technical Digest (online) (Optical Society of America, 2015), paper JT5A.6.
31. M. Choma, M. Sarunic, C. Yang, and J. Izatt, "Sensitivity advantage of swept source and Fourier domain optical coherence tomography," Opt. Express **11**(18), 2183–2189 (2003).
32. P. Meemon, J. Yao, K. S. Lee, K. P. Thompson, M. Ponting, E. Baer, and J. P. Rolland, "Optical coherence tomography enabling non destructive metrology of layered polymeric GRIN material," Sci. Rep. **3**(1), 1709 (2013).
33. S. Ortiz, D. Siedlecki, L. Remon, and S. Marcos, "Optical coherence tomography for quantitative surface topography," Appl. Opt. **48**(35), 6708–6715 (2009).
34. J. Yao, P. Meemon, K. S. Lee, and J. P. Rolland, "Nondestructive metrology by optical coherence tomography empowering manufacturing iterations of layered polymeric optical materials," Opt. Eng. **52**(11), 112111 (2013).
35. J. Yao, P. Meemon, M. Ponting, and J. P. Rolland, "Angular scan optical coherence tomography imaging and metrology of spherical gradient refractive index preforms," Opt. Express **23**(5), 6428–6443 (2015).
36. J. Yao, J. Huang, P. Meemon, M. Ponting, and J. P. Rolland, "Simultaneous estimation of thickness and refractive index of layered gradient refractive index optics using a hybrid confocal-scan swept-source optical coherence tomography system," Opt. Express **23**(23), 30149–30164 (2015).
37. J. Yao, K. P. Thompson, B. Ma, M. Ponting, and J. P. Rolland, "Volumetric rendering and metrology of spherical gradient refractive index lens imaged by angular scan optical coherence tomography system," Opt. Express **24**(17), 19388–19404 (2016).
38. J. Huang, J. Yao, N. Cirucci, T. Ivanov, and J. P. Rolland, "Performance analysis of optical coherence tomography in the context of a thickness estimation task," J. Biomed. Opt. **20**(12), 121306 (2015).
39. S. Choi, M. Yamamoto, D. Moteki, T. Shioda, Y. Tanaka, and T. Kurokawa, "Frequency-comb-based interferometer for profilometry and tomography," Opt. Lett. **31**(13), 1976–1978 (2006).
40. S. K. Chun, H. Jang, S. W. Cho, N. S. Park, and C. S. Kim, "Unfolding displacement measurement method for the aliasing interferometer signal of a wavelength-comb-swept laser," Opt. Express **26**(5), 5789–5799 (2018).
41. K. S. Lee, A. C. Akcay, T. Delemos, E. Clarkson, and J. P. Rolland, "Dispersion control with a Fourier-domain optical delay line in a fiber-optic imaging interferometer," Appl. Opt. **44**(19), 4009–4022 (2005).
42. S. Murali, P. Meemon, K. S. Lee, W. P. Kuhn, K. P. Thompson, and J. P. Rolland, "Assessment of a liquid lens enabled in vivo optical coherence microscope," Appl. Opt. **49**(16), D145–D156 (2010).
43. F. A. Potra and S. J. Wright, "Interior-point methods," J. Comput. Appl. Math. **124**(1–2), 281–302 (2000).
44. G. E. Sommargren, "Embedded fiducials in optical surfaces," U.S. patent 6,014,264 (2000).
45. K. Medicus, J. D. Nelson, and M. Brunelle, "The need for fiducials on freeform optical surfaces," Proc. SPIE **9582**, 958204 (2015).
46. M. Gu, C. Sheppard, and X. Gan, "Image formation in a fiber-optical confocal scanning microscope," J. Opt. Soc. Am. A **8**(11), 1755–1761 (1991).

Optics EXPRESS

47. Y. Zhou, Y. S. Ghim, A. Fard, and A. Davies, "Application of the random ball test for calibrating slope-dependent errors in profilometry measurements," Appl. Opt. **52**(24), 5925–5931 (2013).
48. P. J. Smilie, B. S. Dutterer, J. L. Lineberger, M. A. Davies, and T. J. Suleski, "Design and characterization of an infrared Alvarez lens," Opt. Eng. **51**(1), 013006 (2012).
49. M. Davies, J. Owen, J. Troutman, D. Barnhardt, and T. Suleski, "Ultra-precision diamond machining of freeform optics for the IR," in Imaging and Applied Optics 2015, OSA Technical Digest (online) (Optical Society of America, 2015), paper FM1B.1.
50. J. M. Tamkin, T. D. Milster, and W. Dallas, "Theory of modulation transfer function artifacts due to mid-spatial-frequency errors and its application to optical tolerancing," Appl. Opt. **49**(25), 4825–4835 (2010).
51. K. Liang and M. A. Alonso, "Understanding the effects of groove structures on the MTF," Opt. Express **25**(16), 18827–18841 (2017).
52. T. S. Ralston, D. L. Marks, P. S. Carney, and S. A. Boppart, "Interferometric synthetic aperture microscopy," Nat. Phys. **3**(2), 129–134 (2007).

1. Introduction

During the last decade, the optics manufacturing industry has acquired the capability of fabricating freeform optical quality surfaces for imaging applications owing to the machining flexibility offered by an added third independent servo axis in commercial equipment [1]. This manufacturing advancement drives the emerging development of freeform surfaces that are characterized by their non-rotationally symmetric departures from base spheres. Research has started to show that freeform surfaces allow for considerably extended degrees of freedom in optical design and therefore enable a field of opportunities and innovation in terms of gaining larger fields of view and higher performance, or a significant decrease in volume and weight without compromising the performance. The freeform optical systems are foreseen to be leveraged in the next-generation instruments including wide field of view telescopes [2–4], spectrometers [5], head-worn and heads-up displays [6,7], microscopes, endoscopes, and lithography projection systems, to name a few [8].

An impediment to the broad industrial implementation of freeform surfaces in optical imaging systems is the imminent need of a high performance metrology tool capable of measuring significant surface departures and slopes of the parts. Various area and point surface metrology techniques have been under active investigation so as to extend their capability for optical freeform metrology [9]. Among the current available candidate techniques, tactile coordinate measuring machines (CMMs) are still the industrial workhorse metrology approach for freeform surfaces as a result of their flexibility in measuring complex shapes. Conventional CMMs generally have a large measurement range, however with an uncertainty in the micron level. In order to improve on the precision of CMMs to meet the tolerance of optical freeform surfaces, apart from precision machine design, multi-axis laser interferometric encoders are employed in the scanning axes of a CMM to provide accurate feedback of the position of the stylus with nanometer-class uncertainty. A notable commercial example (UA3P, Panasonic Corporation, Japan) utilizing XYZ frequency-stabilized laser encoders is a "semi-contact" 2D profilometer that employs a highly sensitive atomic force probe with a measuring force ≤ 0.3 mN so as to leave no traceable damage on any surface under test [10]. It is widely recognized that noncontact optical testing is desirable as it eliminates the risks of scratching the test parts and thus extends the types of materials used in manufacturing. The noncontact optical testing techniques being actively pursued are categorized into three main areas: classical interferometry, phase measuring deflectometry, and optical profilometry.

As a prevalent optical testing technique, full field interferometry offers nanometer level precision in testing traditional spherical surfaces. Yet, the challenge of interferometry in testing freeform surfaces arises from the fact that the fringe density created by the slopes of the parts may exceed the Nyquist frequency of the interferometer detectors. Several approaches have thus been developed to enhance the dynamic range of interferometers. In an interferometric null test [11], besides the null lenses, an adaptive optics deformable mirror (DM) [12] or a computer generated hologram (CGH) may alternatively act as the null

Optics EXPRESS

correctors to bring the departure between the test and reference wavefronts within the dynamic range of the interferometer. The accuracy of the measurement highly depends on the quality of the DM or CGH. The current commercial DMs are limited by the actuators to ~80 μm peak-to-valley (PV) departure whereas CGHs incur high-cost customization for each test surface. Moreover, common to all null tests is the extensive alignment and calibration process dedicated for each specific test surface. Another direction as opposed to nulling the non-spherical portion of the test wavefront is to create a lattice of sub-apertures on the test surface (e.g., ZYGO Verifire and QED SSI) such that the measurement within each sub-aperture falls within the dynamic range of an interferometer [13,14]. Advanced stitching algorithms are then applied to form the complete measurement across the full aperture from the collected sub-aperture interferograms [15,16]. One caveat is that the stitching errors may significantly increase with the number of sub-apertures. Other non-null interferometric approaches include lateral shearing interferometry [17], Moire interferometry [18], and tilted wave interferometry configured with a two-dimensional point-source array [19]. Extensive calibrations are generally required to mitigate alignment and ray tracing errors.

Another research focus being actively pursued is deflectometry [20], also known as the reverse Hartmann test [21], structured-light reflection [22] or fringe reflection [23] method. The surface slope is directly measured in deflectometry by analyzing the deformation and displacement of a fringe pattern after being reflected off the test surface. The surface shape is subsequently reconstructed by numeric integration of the slope data. With precision comparable to interferometry, the deflectometric testing systems rely on careful calibration to reach accurate measurements. Moreover, the height ambiguity issue associated with triangulation needs to be addressed, which either adds to the complexity of the system or requires a priori knowledge of a known surface point [20,24].

Finally, 2D optical profilometry shows the potential in measuring complex shapes. Noncontact probes based on high resolution optical techniques such as confocal microscopy [25], white light interferometry [26], and multi-wavelength interferometry [27], combined with mechanical scans may provide means for point-cloud surface profiling. Some notable commercial point-cloud profilometers include the LuphoScan (AMETEK GmbH BU Taylor Hobson/Luphos, Germany) [28], the MarForm MFU200 (Mahr GmbH, Germany) [29], and the UltraSurf 5X (OptiPro Systems, NY, USA) [30]. These instruments may benefit from active tracking to compensate for different measuring distances, which lowers the measurement uncertainty. Their optical probes follow spiral or ring scanning trajectories and stay roughly normal to the test surface. Rigorous calibration of each system needs to be carried out to benchmark their freeform metrology capability.

In light of the ongoing efforts to advance the implementation of freeform optics in commercial optical systems, the metrology component becomes the cost driver of freeform optics manufacturing. Generally affordable metrology tools that reliably meet the tolerance requirement of precision optics manufacturing are in high demand. Other desirable features include expanded instrument universality and reduced operational workload.

In this paper, we investigate a point-cloud method that leverages Fourier-domain swept-source optical coherence tomography (SS-OCT), a technique based on low-coherence interferometry, for precision freeform metrology. As a high-resolution, high-sensitivity and high-speed imaging technique [31], SS-OCT has been utilized for nondestructive material characterization such as qualifying gradient refractive index materials [32–37]. Different optical coherence tomography (OCT) systems with various noise sources have been characterized [38]. In this work, we demonstrate the development of an SS-OCT metrology system for profiling the figure of freeform surfaces. We first investigate the SS-OCT system layout and the methodology for the metrology of surface profiles in Section 2; in Section 3, we develop a comprehensive model that simulates the vertical displacement sensitivity and lateral scanning noise of the system, in order to predict the measurement uncertainty of an arbitrary surface and guide selecting an optimum experimental setup; in Section 4, we

Optics EXPRESS

benchmark the system performance with two traceable standards, and demonstrate the metrology results of an Alvarez freeform surface with 400 μm PV sag; finally, we conclude the paper in Section 5.

2. Method

2.1 System description

We developed a point-cloud metrology system based on SS-OCT. The system is built on a fiber-based Mach-Zehnder interferometer (MZI) configuration as shown in Fig. 1. The light source is a frequency swept laser (HSL-2100-WR, Santec, Japan) centered at 1318 nm with a bandwidth of 125 nm full-width-half-maximum (FWHM). The axial point spread function (PSF) of the system is approximately 10 μm FWHM and the effective frequency sweep rate of the light source is 20 kHz. The swept source has a broader bandwidth than typical frequency comb lasers [39,40], and therefore yields higher displacement detection sensitivity. Light from the source is split by a fiber coupler (90/10) and subsequently delivered to the sample and reference arms of the interferometer. In the reference arm, a Fourier domain optical delay line (FD-ODL) is implemented for dispersion compensation [41]. In the sample arm, collimated light of 3.27 mm $1/e^2$ diameter is focused on a test sample by an objective lens (LCPLN20XIR, Olympus, Tokyo, Japan) with a working NA of 0.178 and a working distance of 8.3 mm. The back-reflected light from a measurement point on the sample and the reference generates spectral interference signals, which are detected by a balanced photo-detector (1817-FC, New Focus, CA, USA) and then digitized on one channel of a 500 MSamples/s, 12-bit analog-to-digital converter (ATS9350, AlazarTech, QC, CA) for further data processing. The detected OCT interference signal is calibrated to the linear frequency space prior to Fourier transform, which is performed by using the time-frequency relation measured by an additional side MZI denoted by a dashed box in Fig. 1. Simultaneously with the detection of the main interference signal, the calibration signal is detected by a second balanced photo-detector and then digitized on a second channel of the same analog-to-digital converter. By performing a Fourier transform of a single recalibrated interference spectrum, a depth-resolved component reflectivity profile along the incident sample beam path is reconstructed. The maximum sensitivity of the system was measured to be 112 dB. The imaging depth range is about 5 mm as determined by a –10 dB sensitivity roll-off.

Note that a unique construction of the SS-OCT freeform-metrology system is a common path setup in the sample arm as will be detailed in Section 2.2. The sample platform that supports the test part and a common path reference flat is mounted on a set of x-y precision motorized linear stages (VP-25XL, Newport, CA, USA) for lateral scanning. The two orthogonal linear stages serve as the fast and slow scanning axes, respectively. For the fast axis, the motorized stage travels at a constant speed and the frame data acquisition is synchronized with the motion of the stage to provide 20 μm scanning spacing; for the slow axis, the translation stage moves at a step increment of 20 μm between the acquisitions of any consecutive fast-scanning frames. The 20 μm lateral sampling resolution was employed for all the data acquisitions reported in this paper. Therefore, for a volumetric imaging field of view of 20 × 20 × 0.5 mm^3 (x,y,z) that captures the entire varying surface profile of an Alvarez freeform surface as will be shown in Section 4.3, 1000 × 1000 × 17,000 (x,y,z) samples were acquired at lateral and axial sampling resolutions of 20 μm and 0.03 μm, respectively. The total scanning time is ~35 minutes for this level of high lateral sampling rate.

It should be noted that dual references are employed in the SS-OCT freeform-metrology system. The original reference mirror in the FD-ODL allows the imaging of both the common path reference and sample simultaneously to guide their alignments for the minimization of aberrations; the common path reference enables mitigating the measurement errors induced

Optics EXPRESS

by the vibrational motions of the translation stages, when the measurements are acquired with the original reference arm being blocked.

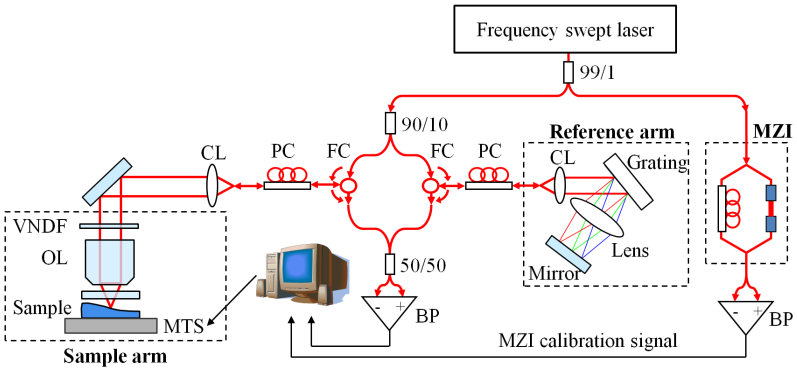

Fig. 1. SS-OCT freeform-metrology system layout. CL: collimating lens; OL: objective lens; PC: polarization controller; FC: fiber circulator; VNDF: variable neutral density filter; MTS: motorized translation stage; BP: balanced photodetector.

2.2 Common path setup

As a point-cloud metrology technique, mitigation of the errors induced in scanning is pivotal to achieving high precision measurements, which may consist of 1) error in measuring the vertical displacement and 2) error in determining the lateral sampling locations. In order to mitigate the first type of errors induced by mechanical scanning as well as the common noise caused by environmental perturbations, a common path setup based on a Mirau-type configuration was constructed and mounted on the x-y motorized translation stages as shown in Fig. 2. A 6-mm thick, λ/20 flatness, transmissive optical window whose bottom surface served as the common path reference was supported by an opto-mechanical cage mount and placed immediately above the test sample. Under the working NA of 0.178, by evaluating the aberrations caused by a BK7 plane parallel plate inserted in the converging sample beam path based on the formulas given in [42], the root-mean-square (RMS) wavefront error at best focus was computed to be 0.016 waves for a 6 mm thick window, which is considered well within the diffraction limit. The on-axis beam eliminates the off-axis aberration types. The axial measurement uncertainty of the system can be significantly improved by the common path interferometric setup that is robust to vibrations and perturbations. Note that a variable neutral density filter is placed in the collimated sample beam path so that, regardless of the sample material types, the back-reflected signals from the sample during point-cloud scanning are always controlled to maximize at ~85% of the saturation level of the photo-detector.

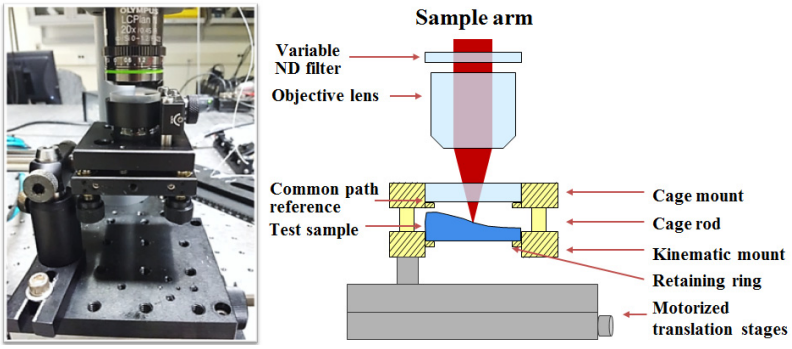

Fig. 2. A photograph and a cross-sectional schematic of a common path setup of the reference flat and test sample simultaneously mounted on x-y motorized translation stages.

Optics EXPRESS

2.3 Lateral scanning field

The second type of scan-induced error, i.e., lateral coordinate errors, may be estimated from the imaging of a calibration standard. A dot grid target with 500 μm spacing and 250 μm dot diameter (Edmund Optics Inc., NJ, USA) was used for the evaluation of the lateral scanning field. The tolerance of the spacing of the dots fabricated by the masked photolithography is better than ± 1 μm.

Figure 3(a) shows a raw gray-scale x-y plane image of the dot grid target acquired by the SS-OCT freeform-metrology system over an imaging region of 18 mm (x) × 20 mm (y). For this imaging, the x and y directions were the fast and slow scanning axes, respectively. A centroiding algorithm was developed to locate the centers of the dots as shown in Fig. 3(b) where the dot grid enhanced in red is overlaid with the detected centroids in blue crosshairs. The estimated horizontal and vertical pixel coordinates of the detected grid of centroids are both 2D matrices consisting of 35 (column) × 39 (row) elements.

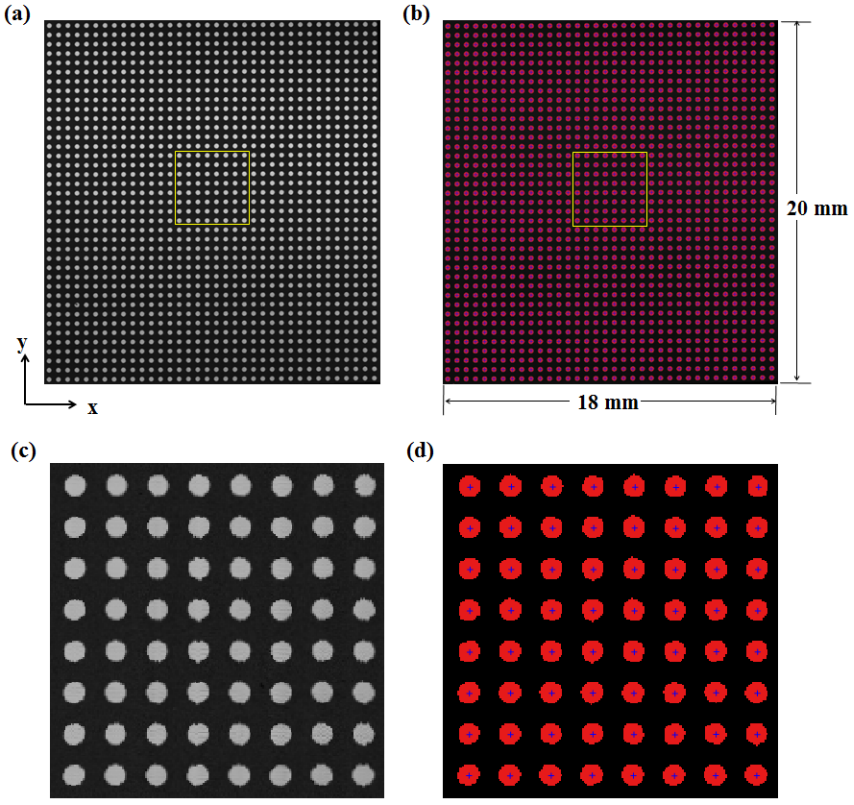

Fig. 3. (a) A raw gray-scale x-y plane image of a dot grid target acquired by the SS-OCT freeform-metrology system. (b) A corresponding image after applying a centroiding algorithm to image (a), which shows the detected centroids (blue crosshairs) of the dots overlaying the dot grid (shown as enhanced red dots). (c) and (d) are enlarged views of the yellow boxes inside (a) and (b), respectively.

Given M columns and N rows, let us denote the column and row indices of a dot as (m, n). The nominal physical centroid location of the dot is described as $x = m \cdot dx$, $y = n \cdot dy$, assuming dx and dy are constants representing the nominal horizontal and vertical separation between neighboring dots. On the other hand, the measured centroid location from the OCT image can be expressed in pixel coordinates as (P_x, P_y). The mapping from (x, y) to (P_x, P_y) reflects the lateral scanning characteristics of the system, and is expressed as $P_x = f_x(x, y)$,

Optics EXPRESS

$P_y = f_y(x, y)$. By analyzing the functions f_x and f_y, the attributes of the lateral scanning field consisting of linearity, orthogonality, straightness, and the sampling resolution are estimated as listed in Table 1. In the formulas, the notation of angle bracket < > with a subscript x or y denotes averaging over the horizontal or vertical direction of the dot array, respectively, to evaluate the mean (i.e., accuracy) and standard deviation (i.e., repeatability).

Table 1. List of criteria and formulas used to evaluate the lateral scanning field from the imaging of the grid target

Evaluation Criterion	Formula
Linearity	
Physical dot locations (x, y) vs. pixel coordinates (P_x, P_y)	$\overline{P_x}(x) = \langle f_x(x, y) \rangle_y$, (1) $\overline{P_y}(y) = \langle f_y(x, y) \rangle_x$. (2)
Orthogonality	
Angle between x and y translation axes with an angle of θ_x and θ_y, respectively, from the horizontal direction of the dot array	$\theta_x = \left\langle \tan^{-1}\left[\frac{\sum_{m=1}^{M}\left(Mf_x(mdx, y) - \sum_{m=1}^{M} f_x(mdx, y)\right)\left(Mf_y(mdx, y) - \sum_{m=1}^{M} f_y(mdx, y)\right)}{\sum_{m=1}^{M}\left(Mf_x(mdx, y) - \sum_{m=1}^{M} f_x(mdx, y)\right)^2} \right] \right\rangle_y$, (3) $\theta_y = \left\langle \tan^{-1}\left[\frac{\sum_{n=1}^{N}\left(Nf_x(x, n\cdot dy) - \sum_{n=1}^{N} f_x(x, n\cdot dy)\right)\left(Nf_y(x, n\cdot dy) - \sum_{n=1}^{N} f_y(x, n\cdot dy)\right)}{\sum_{n=1}^{N}\left(Nf_x(x, n\cdot dy) - \sum_{n=1}^{N} f_x(x, n\cdot dy)\right)^2} \right] \right\rangle_x$. (4)
Straightness	
Deviation in the perpendicular direction from a true line of travel, residual error of $\varepsilon_x(x)$ for x-travel and $\varepsilon_y(y)$ for y-travel	$\varepsilon_x(x) = < f_y(x, y)\cos\theta_x - x\sin\theta_x - \cos\theta_x \frac{\sum_{m=1}^{M} f_y(m\cdot dx, y)}{M} + \sin\theta_x \frac{\sum_{m=1}^{M} f_x(m\cdot dx, y)}{M} >_y$, (5) $\varepsilon_y(y) = < f_x(x, y)\sin\theta_y - y\cos\theta_y - \sin\theta_y \frac{\sum_{n=1}^{N} f_x(x, n\cdot dy)}{N} + \cos\theta_y \frac{\sum_{n=1}^{N} f_y(x, n\cdot dy)}{N} >_x$. (6)
Sampling resolution	
Compute x and y pixel size $dP_x(x)$ and $dP_y(y)$ across the travel range	$dP_x(x) = \langle \frac{dx\cos\theta_x}{f_x(x+dx, y) - f_x(x, y)} \rangle_y$, (7) $dP_y(y) = \langle \frac{dy\sin\theta_y}{f_y(x, y+dy) - f_y(x, y)} \rangle_x$. (8)

Linearity is evaluated from the relation of x (or y) vs. P_x (or P_y) as shown in Eq. (1) (or Eq. (2)). The results of mean x (or y) vs. mean P_x (or P_y) averaged along columns (or rows) are plotted in Figs. 4(a) and 4(b), respectively, with the error bars denoting the standard deviations. Both plots show good linearity in the identified pixel numbers of the centroids, which are consistent with nominal specifications.

Furthermore, another aspect of the lateral scanning quality to consider is the orthogonality of the two nominally perpendicular, fast and slow scanning axes. Therefore, the (P_x, P_y) pixel coordinates of every row (or column) of detected centroids were linearly fitted. From the

Optics EXPRESS

slope of the least-squares fit lines, the angle between the horizontal direction of the dot array and the x (or y) translation axis of the motor, θ_x (or θ_y), was calculated based on Eq. (3) (or Eq. (4)). For perfectly aligned, orthogonal x-y motion axes, $\theta_y - \theta_x = \pi/2$; any deviation from $\pi/2$ shows an orthogonality error. A 0.289° (σ = 0.004°) deviation angle from orthogonality between the x and y scanning axes was measured for the SS-OCT freeform-metrology system. Numerical correction for this orthogonality error was applied to all point cloud data collected by the x-y stage set as a standard calibration procedure.

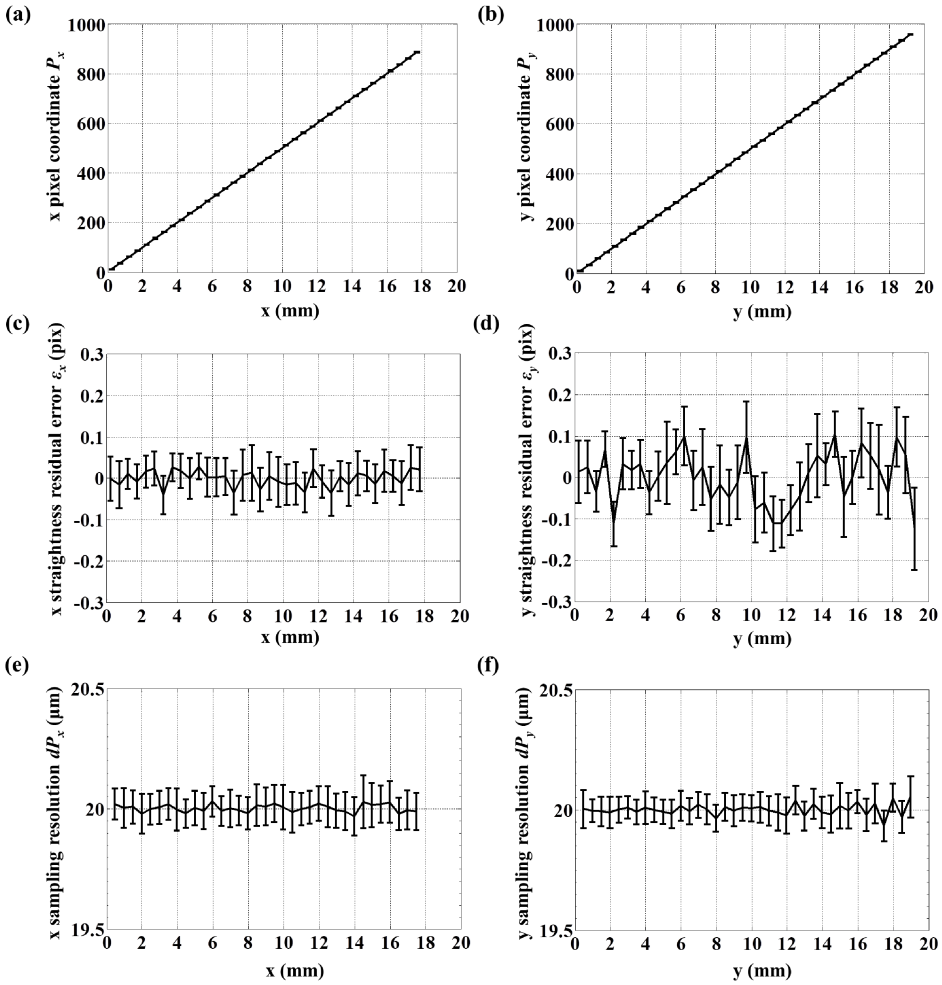

Fig. 4. The nominal physical x coordinates of the centroids vs. (a) the detected x pixel numbers of the centroids averaged column-wise, (c) the linear fitting residuals of x dot grid lines averaged over all rows, and (e) the computed x pixel resolutions averaged column-wise. The nominal physical y coordinates of the centroids vs. (b) the detected y pixel numbers of the centroids averaged row-wise, (d) the linear fitting residuals of y dot grid lines averaged over all columns, and (f) the computed y pixel resolutions averaged row-wise.

From the same linear fitting that calculates the orthogonality of the stage set, straightness of the linear stages can be simultaneously evaluated based on the residual error after fitting. Computed by Eqs. (5) and (6), the fitting residuals of all rows (or columns) were averaged. The yielded means, denoted as $\varepsilon_x(x)$ for row-wise fitting or $\varepsilon_y(y)$ for column-wise fitting, along with the associated standard deviations are plotted in Figs. 4(c) and 4(d), respectively. The RMS fitting residuals were estimated to be on average 0.05 pixels along the x scanning

axis (fast axis), and 0.085 pixels along the y scanning axis (slow axis). The observed straightness residuals of both the fast and slow scanning axes are within 2 μm RMS. The slight deterioration in the straightness along the vertical dot grid lines (corresponding to the direction of the slow scanning axis) is attributed to the inevitable precision error in synchronizing the start of the frame data acquisition with the motion of the fast scanning stage.

Finally, the sampling steps of lateral scanning in both x and y directions are evaluated. The projection of the nominal x spacing between two neighboring dots along the x-motor direction, i.e., $dx \cdot \cos\theta_x$, is divided by the differences in the P_x coordinates of every pair of adjacent centroids in a row to yield the estimated x pixel sampling step dP_x. This calculation as shown in Eq. (7) was performed for all the 39 rows; the means and standard deviations of the x pixel sampling step averaged over the 39 rows are shown in Fig. 4(e). The x pixel sampling step was estimated to be 20.002 ± 0.016 μm. Similar analysis procedures were conducted for estimating the y pixel sampling step as shown in Eq. (8); the results are plotted in Fig. 4(f). The y pixel sampling step was estimated to be 20.001 ± 0.023 μm. The x and y scanning axes show good consistency, accuracy, and precision of the sampling, as compared to a theoretical lateral sampling step of 20 μm set in both directions.

2.4 Data processing

The data acquisition and processing procedures will now be discussed. As shown in Fig. 5, at each (x,y) coordinate, an SS-OCT interference spectrum is collected. During the data processing, a Fourier transform is performed on a spectrum to yield a depth profile, where the peak location and amplitude of an axial PSF correspond to the depth (i.e., z axis) position and the field reflectivity of the test sample, respectively. Synchronously with the lateral x-y scanning of the test sample, spectra are acquired from a well-calibrated, nearly rectangular grid of points on the test sample. By applying a peak detection algorithm to identify the locations of the PSFs across all the corresponding depth profiles, a point cloud measurement covering the surface sag profile of the test sample is then collected. The measurement is further cropped to approximately the effective aperture of the part.

The collection of point cloud data after cropping is mathematically written as $D_0^{(i)} = \{x_0^{(i)}, y_0^{(i)}, z_0^{(i)}\}^T{}_{i=1,2,\ldots Q}$ where Q is the number of data points. To register the measurement with the nominal form of the test sample, rigid body transformations of the measured surface profile are allowed in six degrees of freedom, namely, the yaw, pitch, roll rotation angles α, β, γ, and the x, y, z translations x_t, y_t, z_t. Therefore, the point cloud collection after rigid body transformation, denoted as $D_1^{(i)} = \{x_1^{(i)}, y_1^{(i)}, z_1^{(i)}\}^T{}_{i=1,2,\ldots Q}$, can be expressed as

$$D_1^{(i)} = \{x_1^{(i)}, y_1^{(i)}, z_1^{(i)}\}^T = R_z(\alpha)R_y(\beta)R_x(\gamma)D_0^{(i)} + T(x_t, y_t, z_t), \tag{9}$$

where the yaw, pitch, roll, and translation matrices are

$$\begin{aligned} R_z(\alpha) &= \begin{bmatrix} \cos\alpha & -\sin\alpha & 0 \\ \sin\alpha & \cos\alpha & 0 \\ 0 & 0 & 1 \end{bmatrix}, R_y(\beta) = \begin{bmatrix} \cos\beta & 0 & \sin\beta \\ 0 & 1 & 0 \\ -\sin\beta & 0 & \cos\beta \end{bmatrix}, \\ R_x(\gamma) &= \begin{bmatrix} 1 & 0 & 0 \\ 0 & \cos\gamma & -\sin\gamma \\ 0 & \sin\gamma & \cos\gamma \end{bmatrix}, \; T(x_t, y_t, z_t) = \begin{bmatrix} x_t \\ y_t \\ z_t \end{bmatrix} [1,1....1]_{1\times Q}. \end{aligned} \tag{10}$$

An interior-point nonlinear optimization algorithm [43] is implemented to drive the search of the combination of $[\alpha, \beta, \gamma, x_t, y_t, z_t]$ that seeks the global minimum of the root-mean-square

deviation (RMSD), known as the RMS of the residual profile. This objective function is mathematically defined as $\sqrt{\frac{\sum_{i=1}^{Q}(f(x_1^{(i)},y_1^{(i)})-z_1^{(i)})^2}{Q}}$, where the function f denotes the nominal equation for surface sag. The identified global minimum condition of RMSD yields an optimum registration of the measurement with the prescription.

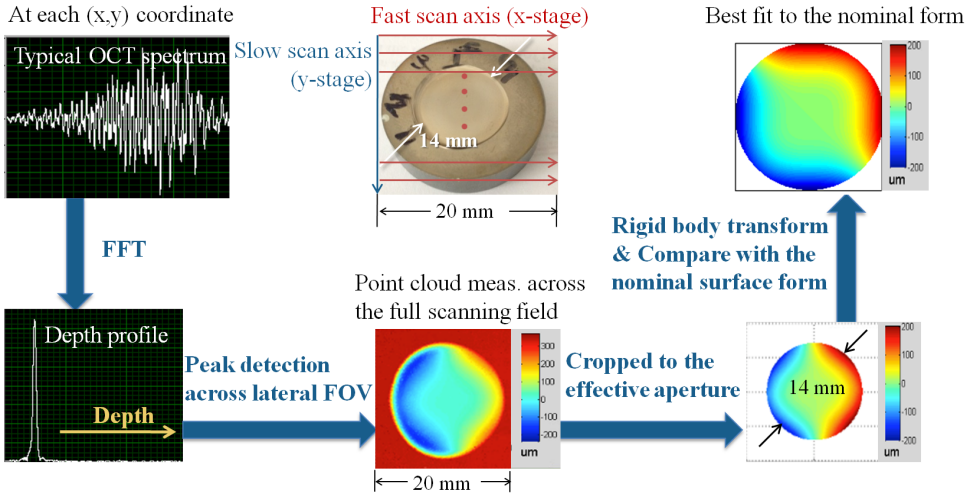

Fig. 5. Data processing procedures for SS-OCT freeform metrology.

With the OCT technique, peripheral or potentially certain sub-surface alignment fiducials [44] may also be readily imaged together with the freeform surfaces under test to guide establishing a universal coordinate system. Adding fiducials will eliminate the need of rigid body transformations in matching the point cloud to the prescription [45], and allow direct, unambiguous transfer of the metrology result to the system alignment and assembly process.

3. System modeling

Based on the SS-OCT freeform-metrology system described in Section 2, we developed a comprehensive model of the system that accounts for the various noise sources and predicts the system uncertainty in measuring a freeform surface.

In Sections 3.1 – 3.3, we investigate the three separate signal-to-noise ratio (SNR) roll-off factors that affect the system sensitivity in single-point vertical displacement sensing: sample depth, defocus distance, and slope. We show that the SS-OCT system provides unbiased estimation of the sag departure; therefore, only the precision errors, which are determined by the SNR and represented by the standard deviation across multiple measurements, are characterized and used interchangeably with the word 'uncertainty' in the rest of the simulation section.

In addition to the vertical displacement detection sensitivity, a second contributor to the point-cloud surface metrology uncertainty is the lateral scanning noise that was previously evaluated in Section 2.3. With the foundations of the system SNR modeling built, the overall measurement uncertainty map of an arbitrary sample under test can be predicted, with a couple of examples shown in Section 3.4. Predicting uncertainty maps via modeling allows the investigation of optimum experimental conditions.

3.1 Measurement uncertainty affected by depth

Inherent to an FD-OCT system is its sensitivity (hence SNR) roll-off with depth (depth being defined as the optical path difference between the sample and reference paths). In SS-OCT,

Optics EXPRESS

this roll-off is attributable to the finite instantaneous linewidth of the swept source. The convolution of the lineshape function with the spectral interferogram leads to the multiplication of the axial PSF with a fall-off curve through depth in the Fourier-transformed z-space. We experimentally measured the system sensitivity decay with depth and plot in Fig. 6(a) the peak intensities of the axial PSFs through a depth range of 5 mm at every 100 µm intervals. The signal power was normalized by its maximum at the first measured depth of ~20 µm instead of the zero to avoid the proximity of the DC term. It can be seen from the figure that the signal drops by about –10 dB at 5 mm depth.

The sensitivity decay with depth causes an increase in the measurement uncertainty when determining the depth of back-reflections captured by SS-OCT. To quantitatively predict the uncertainty increase trend, we established a model in simulation that accounted for the sensitivity roll-off with depth and the noise sources of the A-scan trigger jitter, the source intensity noise, and the detector noise. Detailed mathematical descriptions of the noise model are provided in reference [36].

A set of 1000 interference spectra was then simulated for measuring a point on a flat surface placed at every 100 µm depth up to 1 mm (except for the first depth being at 20 µm instead of zero), with Gaussian random noise generated by the model to represent a realistic distribution of 1000 measurements conducted repeatedly in experiment. The spectra were then zero-padded and Fourier-transformed (axial sampling resolution of ~2 nm), and peak detection was performed to extract the depth location of the sample surface. The mean and standard deviation of the measured surface depth across the 1000 simulated repeated measurements over the 1 mm depth range are plotted in Figs. 6(b) and 6(c), respectively. As shown in Fig. 6(b), the agreement of the mean measured depth averaged from 1000 measurements with the ground truth set in simulation to within 10 nm (on average 2 nm) proved the validity of the system and associated algorithms in providing accurate measurements of the sag departure of a single point on a surface. As shown in Fig. 6(c), the simulation predicted an increase in measurement uncertainty from ~3 nm (20 µm depth) to ~62 nm (1 mm depth), showing a quasi-linear trend over the 1 mm range. The slope of the measurement uncertainty curve is ~6 nm per 100 µm increased depth.

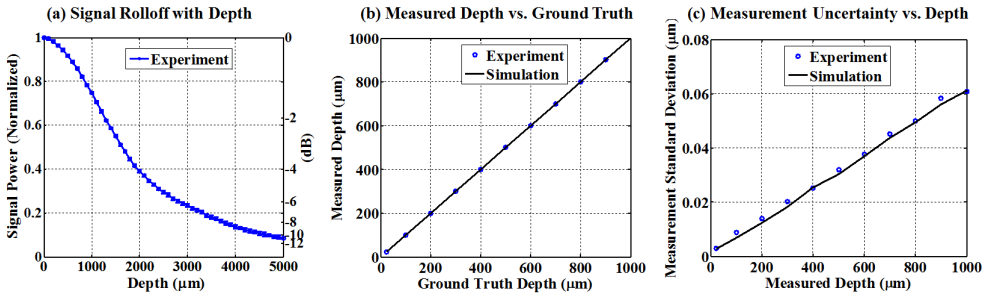

Fig. 6. (a) Experimentally measured decay of sensitivity (with error bars) in SS-OCT across 5 mm depth range. (b) Consistency of the measured depth with the ground truth. (c) Increased measurement uncertainty as a function of the increasing measured depth.

To verify the simulation, we also experimentally acquired 11 sets of 1000 spectra from an optical flat placed at every 100 µm depth up to 1 mm optical path difference (OPD) relative to the reference arm (except for the first measured depth being at 20 µm). The reference mirror was translated by a linear motorized stage to create varying OPDs between the two arms, and the optical flat was kept at focus to rule out any effect induced by focus changes. The experimental results in measuring the depth of the flat surface were consistent with the simulation predictions as shown in Figs. 6(b) and 6(c). The results indicate the effectiveness of the model in estimating the depth-dependent precision of the SS-OCT metrology system.

Optics EXPRESS

3.2 Measurement uncertainty affected by defocus distance

As seen in the last section, the SNR of acquired SS-OCT data affects the precision in determining the axial location of a back-reflection signal. Besides placing a test surface at a depth close to zero-delay-line, higher SNR is achieved by focusing the objective lens on the surface. With the increasing distance of a test surface away from the focus of the objective lens, the peak amplitude of the axial PSF follows a fall-off curve shown in Fig. 7(a). The blue curve was experimentally sampled by measuring the top surface of a fixed optical flat and translating the objective (working NA of 0.178) at every 10 μm axially to form defocus distances of 0 – 1 mm, which fits the theoretical fall-off curve in black [46].

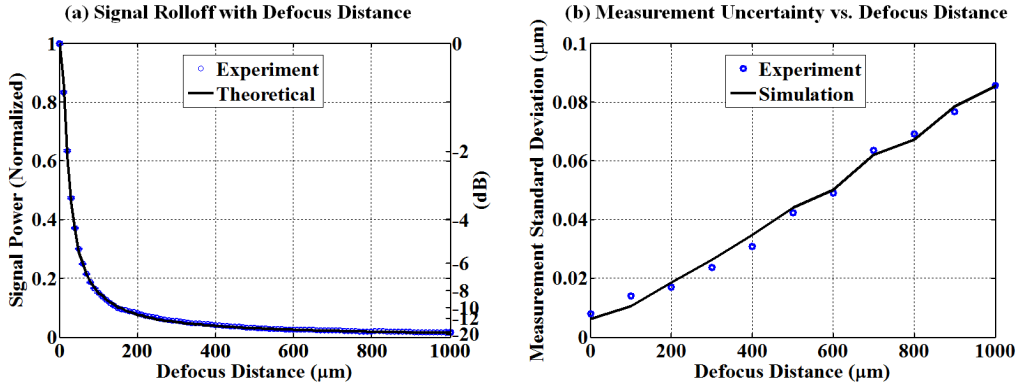

Fig. 7. (a) Theoretical and experimentally-measured (with error bars) signal decay in SS-OCT with the increased distance up to 1 mm from the optical flat to the focus of the objective lens. (b) Increased measurement uncertainty in locating the sample surface placed at 50 μm depth with the increased defocus distance (i.e., signal decay).

To evaluate the uncertainty associated with locating the axial position of a PSF in SS-OCT affected by the rapidly decreasing signal amplitude as a result of the defocus distance from the objective lens, we simulated SS-OCT spectral interference signals from measuring a point on a flat surface (placed at 50 μm depth) collected at defocus distances ranging from 0 – 1 mm at every 100 μm interval guided by the PSF amplitude fall-off curve. A set of 1000 interference spectra were generated at each defocus distance with the same noise model in Section 3.1 applied to simulate repeated measurements. Processing algorithms were applied to find the axial locations of the yielded PSFs. The standard deviations of the differences from the ground truth 50 μm depth across 1000 simulated repeated measurements are plotted in Fig. 7(b) through the 0 – 1 mm defocus distances modeled, which shows an increase from ~6 nm to ~85 nm, while the amplitude of the PSF decays by –18 dB.

Meanwhile, we also experimentally acquired SS-OCT data sets from an optical flat, each set consisting of 1000 repeated spectra, at the same range of defocus distances by translating the objective lens with a precision motorized stage. The standard deviations of the 1000 experimental measurements at each defocus distance are plotted against the simulation results in Fig. 7(b), which shows close agreement.

3.3 Measurement uncertainty affected by slope

A third SNR fall-off factor critical to the testing of freeform surfaces is the local slope of the surface under test. With increasing slope, the amount of back-reflected signal re-collected by the SS-OCT system decreases, and therefore the measurement precision degrades.

3.3.1 Slope dependency of back-reflected signal

To quantitatively estimate the amount of signal fall-off with slope, we first look at the case from a geometrical ray tracing point of view. Figure 8(a) shows a schematic view of the ray

Optics EXPRESS

path of a focused light cone reflected by a sloped surface with an inclination angle α. $\overline{DH}$ represents the exit pupil of the optical system. Denoting the numerical aperture as *NA*, the half apex angle of the light cone is therefore $\theta = \sin^{-1}(NA)$. The normal of the surface under test is $\overline{EI}$. Upon specular reflection, the chief ray of the ray bundle changes from $\overline{GI}$ to $\overline{IC}$, where $\angle GIE = \angle EIC = \alpha$. It can be seen that when $\alpha < \theta$, a portion of the reflected light cone falls within the numerical aperture of the objective lens and is returned to the optical system, as shown by the shaded triangle ΔDFI in Fig. 8(a). To estimate the amount of return signal, the incident and reflected light cones are projected onto the same x-y plane as the exit pupil as shown in Fig. 8(b). Therefore, the photon flux flowing through the solid angle extended by the overlapping, shaded area in Fig. 8(b) as compared to that through the entire area of ellipse C_1 represents the portion of back-reflected signal collected by the SS-OCT system.

So far we have treated the model from a geometrical ray tracing perspective; next, the Gaussian irradiance profile of the laser beam needs to be considered. The reflected beam irradiance across ellipse C_1 can be described by a Gaussian function as

$$I(r, z') = \frac{c}{w^2(z')} \cdot e^{-\frac{2r^2}{w^2(z')}}, \tag{11}$$

where *c* is a constant, *z'* is the axial distance from the beam waist located at *I* (noting the optical axis change from *z* to *z'* direction upon reflection), *r* is the radial distance from the center axis of the beam, and *w(z')* is the radius where the beam irradiance falls to $1/e^2$ of the axial value at the plane *z'*. Denoting the Rayleigh distance as z_R and Gaussian beam waist radius as w_0, *w(z')* can be expressed as

$$w(z') = w_0 \sqrt{1 + \left(\frac{z'}{z_R}\right)^2}. \tag{12}$$

Switching to polar coordinates (r, φ) with the polar origin residing at C_1, the x-y plane shown in Fig. 8(b), which contains the ellipse C_1 and circle C_2, can be expressed as

$$z' = -\tan(2\alpha) \cdot r\cos\varphi + \frac{f}{\cos(2\alpha)}, \tag{13}$$

where f is the focal length of the objective lens.

Combining Eqs. (11) – (13), the reflected beam irradiance distribution across ellipse C_1 is described in polar coordinates (r, φ) as

$$I(r,\varphi) = \frac{c}{w_0^2\left[1 + \left(\frac{\tan(2\alpha)}{z_R} \cdot r\cos\varphi - \frac{f}{z_R\cos(2\alpha)}\right)^2\right]} \cdot e^{-\frac{2r^2}{w_0^2\left[1 + \left(\frac{\tan(2\alpha)}{z_R} \cdot r\cos\varphi - \frac{f}{z_R\cos(2\alpha)}\right)^2\right]}}. \tag{14}$$

Optics EXPRESS

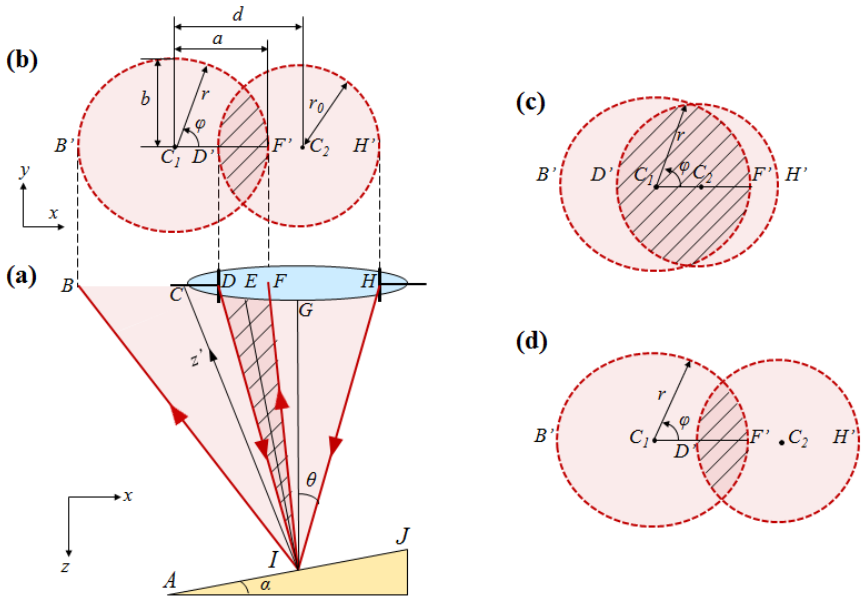

Fig. 8. Illustration of the geometry of the light cones incident and reflected by a surface with an inclination angle α. (a) and (b) are x-z and x-y cross-sectional views of the geometry, respectively. (c) and (d) illustrate two different cases in the calculation of the back-reflected signal re-collected by the SS-OCT system, depending on the surface inclination angle α. The shaded areas in all graphs represent the portion of back-reflected light captured by the objective lens.

Next, we calculate the radiant flux of the back-reflected signal P_{in} that is the portion collected back by the SS-OCT system. P_{in} can be expressed by an integral over the shaded area denoted as (σ), as

$$P_{in} = \iint_{(\sigma)} I(r,\varphi) r dr d\varphi. \tag{15}$$

To further mathematically express the domain of integration, the equations for ellipse C_1 and circle C_2 are written out in Eqs. (16) and (17), respectively, as

$$\left(\frac{r\cos\varphi}{a}\right)^2 + \left(\frac{r\sin\varphi}{b}\right)^2 = 1, \tag{16}$$

where a and b are the semi major and minor axes of the ellipse C_1, respectively; and

$$(r\cos\varphi - d)^2 + (r\sin\varphi)^2 = r_0^2, \tag{17}$$

where r_0 is the radius of the circle C_2, and d is the distance of $\overline{C_1C_2}$.

As shown in Fig. 8(a), a, b, and d may be linked with the inclination angle of the sloped surface under test, α, and the half-angle of the light cone, θ, by the following equations

$$a = f\frac{\tan(2\alpha+\theta) - \tan(2\alpha-\theta)}{2}, \tag{18}$$

$$b = f\frac{\tan\theta}{\cos 2\alpha}, \tag{19}$$

Optics EXPRESS

$$d = f\frac{\tan(2\alpha+\theta)+\tan(2\alpha-\theta)}{2}. \tag{20}$$

Based on the Eqs. (16) and (17) for ellipse C_1 and circle C_2, respectively, the surface integral over (σ) in Eq. (15) can be explicitly written out as

$$P_{in} = \begin{cases} 2\int_0^{\phi_i} d\varphi \int_0^{\frac{ab}{\sqrt{a^2\sin^2\varphi+b^2\cos^2\varphi}}} I(r,\varphi) r dr \\ +2\int_{\phi_i}^{\pi} d\varphi \int_0^{d\cos\varphi+\sqrt{r_0^2-d^2\sin^2\varphi}} I(r,\varphi) r dr \end{cases}, \quad if\ d \le r_0$$

$$P_{in} = \begin{cases} 2\int_0^{\phi_i} d\varphi \int_{d\cos\varphi-\sqrt{r_0^2-d^2\sin^2\varphi}}^{\frac{ab}{\sqrt{a^2\sin^2\varphi+b^2\cos^2\varphi}}} I(r,\varphi) r dr \\ +2\int_{\phi_i}^{\sin^{-1}(\frac{r_0}{d})} d\varphi \int_{d\cos\varphi-\sqrt{r_0^2-d^2\sin^2\varphi}}^{d\cos\varphi+\sqrt{r_0^2-d^2\sin^2\varphi}} I(r,\varphi) r dr \end{cases}, \quad if\ d > r_0 \tag{21}$$

where ϕ_i corresponds to the polar angle of the upper point of intersection of ellipse C_1 and circle C_2, and $\phi_i = \tan^{-1}\left(\frac{-b^2(a^2b^2-a^4+b^2d^2-b^2r_0^2+a^2d^2+a^2r_0^2-2ad\sqrt{-a^2b^2+a^2r_0^2+b^4+b^2d^2-b^2r_0^2})}{a^2d-a\sqrt{-a^2b^2+a^2r_0^2+b^4+b^2d^2-b^2r_0^2}}\right)$. Note that the surface integral carries different forms for the cases of $d \le r_0$ or $d > r_0$; representative illustrations of the two different cases are shown in Figs. 8(c) and 8(d), demonstrating a transition in the size of the overlapping region between ellipse C_1 and circle C_2 with a change in the angle α of the slope under test.

The back-reflected signal re-collected by the optical system has been established as a function of the slope under test. By numerically evaluating the integrals in Eq. (21), this relation is plotted in Fig. 9(a). Note that the signal in the vertical axis is normalized by the total amount of reflected light (i.e., total radiant flux through ellipse C_1); in other words, the light reflected by a zero-slope surface and re-entering the numerical aperture of the objective lens is denoted as unity. Corresponding to an objective lens with NA = 0.178, the maximum detectable slope without signal cut-off is 10.25°.

3.3.2 Simulation of slope-dependent measurement uncertainty

In Section 3.3.1, the physical model of SNR roll-off with the increasing slope of the test surface has been established, which leads to the third factor affecting the precision in measuring a freeform surface. To quantitatively estimate the level of measurement precision degradation as a result of the increasing slope, we simulated SS-OCT spectral interference signals back-reflected from a point (placed at 50 μm depth) on a test surface pivoting about the focus of the objective lens with an inclination angle ranging from 0 – 10° (at every 0.1° increment). The amplitude of the interference spectrum follows the signal fall-off curve shown in Fig. 9(a), as different measurement slopes were simulated. Based on the same noise model as in Section 3.1, a set of 1000 interference spectra with Gaussian random noise injected were statistically generated for each measurement slope. The standard deviations of the sag departure across 1000 simulated repeated measurements are plotted in Fig. 9(b). The measurement precision is estimated to be 6 nm for a 5° slope and 495 nm for a 10° slope. Note that this prediction isolates the sole effect from the change in the test slope, since the test surface is kept at a constant depth of 50 μm and always at the focus of the objective lens.

Optics EXPRESS

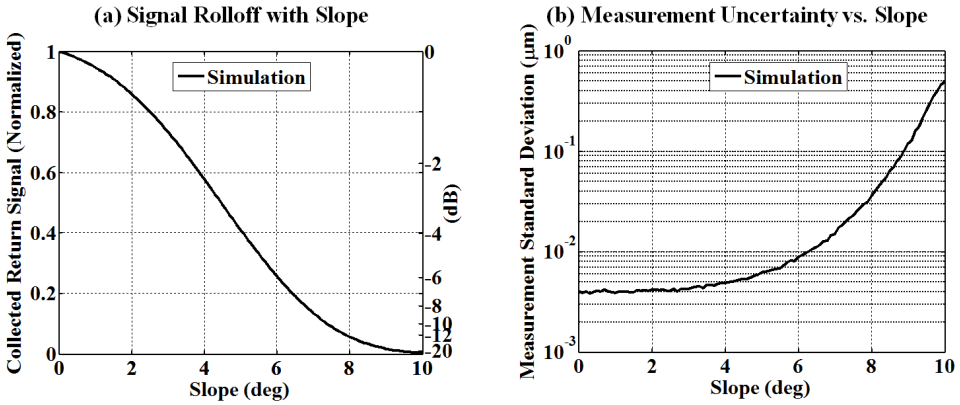

Fig. 9. (a) Theoretical signal decay in SS-OCT with increased slope of the test surface. (b) Simulated increased measurement uncertainty in locating the sample surface placed at 50 μm depth and at focus with the increased slope of the test surface.

3.4 Estimation of overall measurement uncertainty

In Sections 3.1 – 3.3, we have described an important framework of our model that accounts for the three SNR fall-off factors impacting the measurement precision of vertical displacements in surface metrology. Regarding an arbitrary combination of the depth location, focus condition, and slope of any point on a freeform surface, the model can predict the corresponding measurement precision of the sag departure. Combined with additional modeling of the lateral scanning noise as described in Section 2.3, the simulation engine enables mapping the surface metrology uncertainty of the entire freeform point cloud.

Meanwhile, it can be seen that for a freeform surface with defined sag and slope profiles, the point-cloud measurement uncertainty map remains to be affected by where the zero-optical-delay plane and the focal plane are located. In simulation, the impact of these two factors on the mean value of the point-cloud measurement uncertainty map, a figure of merit that we seek to minimize, can be investigated and provide guidance to the optimum experimental setup. Two examples will be shown in Sections 3.4.1 and 3.4.2.

3.4.1 Simulation of baseline spherical surface

A spherical surface naturally provides a continuous range of slopes to be tested. In the laboratory, we have a grade 5 spherical ball standard with a nominal radius of curvature of 12.7 mm and surface roughness < 5 nm (i.e., Caliball, Optical Perspectives Group, AZ, USA). Prior to experimental measurements of this standard, the surface metrology uncertainty was estimated in simulation as a baseline. Recall that corresponding to the SS-OCT objective lens working NA of 0.178, a specular reflection signal may be collected from up to ~10° in slope. However, to avoid the significant SNR degradation near the cutoff slope, we limit the region of interest (ROI) to a spherical cap with edge slope of 8.4° where ~15 dB slope-induced signal roll-off compared to normal incidence is estimated from Eq. (21). The ROI, which encompasses a dome with a radius of ~1.85 mm, will be characterized by both simulation here and experiment later in Section 4.2. Note that a common-path reference is always set at 50 μm depth from the zero-optical-delay plane.

Figure 10(a) shows in a contour plot the estimated mean surface measurement uncertainty as a function of the z locations of the focal plane and the zero-optical-delay plane, with z = 0 referencing to the plane tangent to the apex of the Caliball as illustrated in Fig. 10(b). The valley of the contour plot is denoted by an orange star. This points to an optimum experimental setup of focal plane at z = 100 μm and zero-optical-delay plane at z = –110 μm, which is estimated to yield a mean surface measurement uncertainty of ~154 nm across the ROI. Figure 10(c) shows the corresponding simulated, surface measurement uncertainty map

Optics EXPRESS

under this optimum condition. As expected, the repeatability degradation with increased slope is clearly observed. The simulation of Caliball, despite not a freeform surface, serves as a baseline to demonstrate how the metrology system may perform in terms of measuring mild to moderate slopes on an actual optical surface.

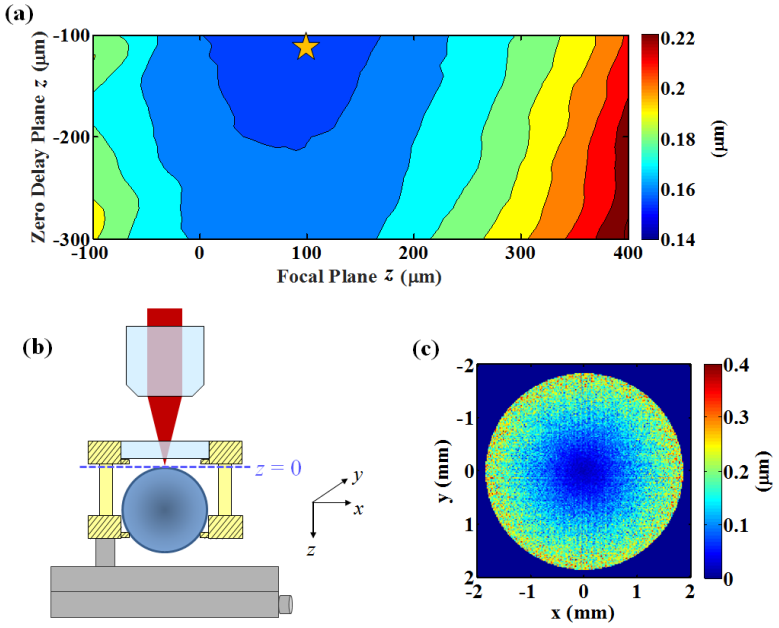

Fig. 10. (a) Contour plot of the mean surface measurement uncertainty as a function of the z locations of the zero-optical-delay plane and focal plane. The orange star denotes the valley of the plot. (b) illustrates the location of the z = 0 reference plane with respect to the Caliball. (c) Simulated surface uncertainty map under the specific focus and sample depth conditions denoted by the orange star in (a).

3.4.2 Simulation of an Alvarez freeform surface

A freeform sample that we examine in this paper is a germanium Alvarez surface, which has a 14 mm circular clear aperture with the surface function given by an x-y polynomial of 3rd order as

$$z(x,y) = 0.000566\left(x^3 + y^3\right)(mm). \tag{22}$$

The measurement results of the Alvarez freeform surface will be shown in Section 4.3. Prior to that, we evaluated in simulation the optimum experimental condition that would minimize the mean surface measurement uncertainty of this freeform surface.

Figure 11(a) shows a contour plot of the estimated mean surface measurement uncertainty versus the z locations of the focal plane and the zero-optical-delay plane. Figure 11(b) illustrates the location of z = 0 as calculated from Eq. (22). The optimum combination of focal plane at z = –200 μm and zero-delay plane at z = –300 μm is denoted by an orange star that's at the valley of the contour plot in Fig. 11(a). Under this optimum condition, the predicted surface measurement uncertainty map across the ROI of 7 mm radius is shown in Fig. 11(c), which shows a minimized average uncertainty of ~61 nm.

Optics EXPRESS

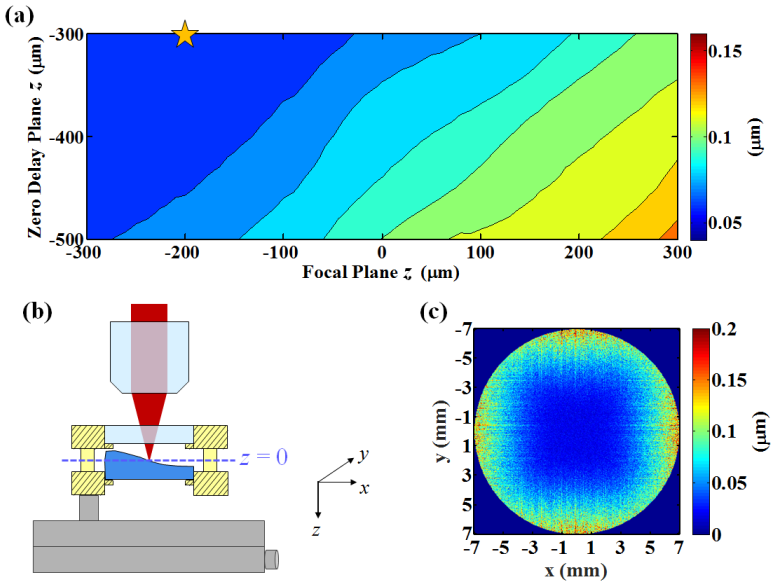

Fig. 11. (a) Contour plot of the mean surface measurement uncertainty as a function of the z locations of the zero-optical-delay plane and focal plane. The orange star denotes the valley of the plot. (b) illustrates the location of the z = 0 reference plane with respect to the Alvarez surface. (c) Simulated surface uncertainty map under the specific focus and sample depth conditions denoted by the orange star in (a).

4. Experimental results

In this section, we first experimentally benchmarked the performance of the SS-OCT surface metrology system using traceable standards of an optical flat and a spherical standard in Sections 4.1 and 4.2, respectively. In Section 4.3, the results of measuring an Alvarez freeform surface will be discussed.

4.1 Optical flat

As discussed in Section 2.2, a unique feature of the SS-OCT metrology system is the common path setup. To test the effectiveness of the common path layout in response to axial jitter motions of the translation stages, the SS-OCT metrology system was used to measure a plane mirror with λ/20 surface flatness. As shown in Fig. 12(b), the measured surface profile of the flat across an area of 20 mm in diameter shows an RMS error of 12 nm and PV error of 69 nm. The small residual profile deviating from an ideal plane is dominated by astigmatism figure error, which was confirmed by a conventional laser Fizeau interferometry test as shown in Fig. 12(c). In large part, the common path configuration is shown to mitigate the sample OPD fluctuations caused by axial jitters.

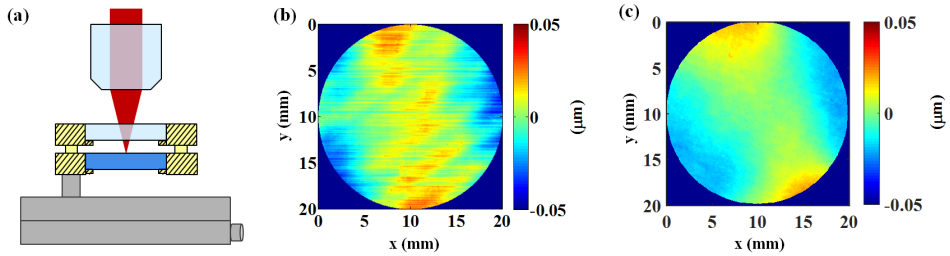

Fig. 12. Using the common path setup schematically shown in (a), the surface profile of a λ/20 plane mirror measured by the SS-OCT system is shown in (b). A laser Fizeau interferometry test result of the same mirror is shown in (c).

Optics EXPRESS

4.2 Spherical standard

The Caliball simulated in Section 3.4.1 was also measured by the SS-OCT system using the optimum focal and depth conditions predicted by simulation. Five repeated measurements of the spherical cap ROI with a radius of 1.85 mm were conducted against a common path reference as shown in Fig. 13(a). The radius of curvature of the Caliball was measured to be 12.701 ± 0.021 mm. Each measurement was registered with the nominal surface figure. The average residual profile in sag is shown in Fig. 13(b), which has an RMSD of 154 nm. The RMSD reflects on the fact that the Caliball is not a perfect sphere, and the residual departure may be further mitigated when increasing the number of random ball test repetitions [47].

On the other hand, the standard deviation profile computed from the five measurements is shown in Fig. 13(c), which is on average 152 nm over the measured ROI. This result is in close agreement with the standard deviation map predicted by the simulation model, showing an average of 154 nm (see Section 3.4.1).

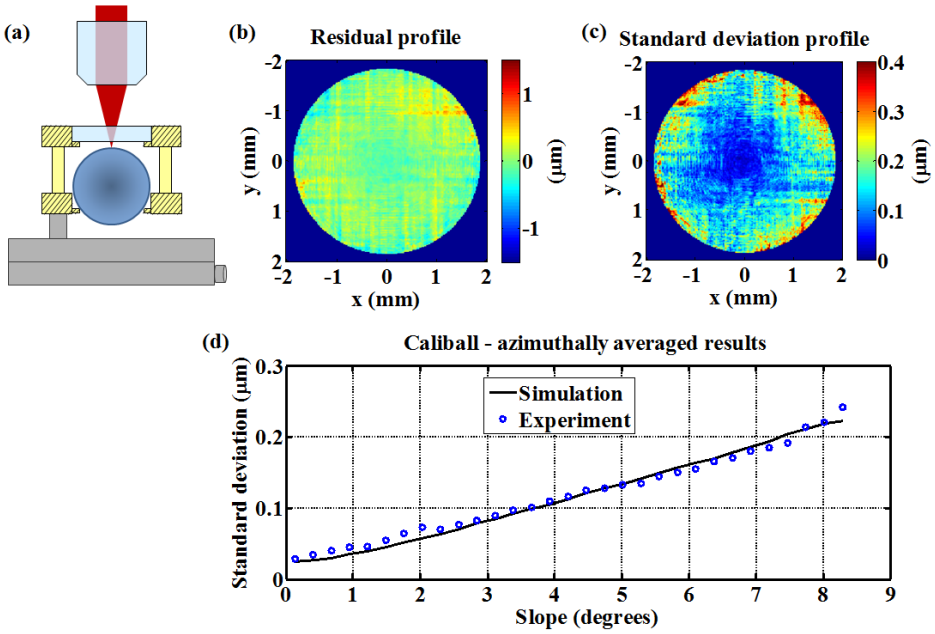

Fig. 13. An R = 12.7 mm Caliball is measured by the SS-OCT metrology system using the common path setup schematically shown in (a). Within the imaging ROI of 1.85 mm radius, the residual profile of the Caliball after subtracting out its nominal form is shown in (b). The standard deviation profile across five repeated measurements is shown in (c). (d) The standard deviation map in (c) is azimuthally averaged in 60 μm wide annuli and plotted as a function of the mean slope of the analysis annuli to demonstrate slope-dependent measurement precision (blue dots), which agrees with simulation results (black curve).

As seen in Fig. 13(c), rotational symmetry of the plot is expected with an increased number of repeated measurements, showing slope-dependent precision degradation. To quantitatively assess the measurement precision as a function of the increasing slope from the center to the periphery of the ROI, the standard deviation profile in Fig. 13(c) was further azimuthally averaged within each of a range of 60 μm wide annular rings that were concentric about the apex (defined as the point of normal beam incidence) and varied in diameter increasingly. The azimuthally-averaged standard deviations are plotted as a function of the mean slope of the analysis annuli as shown by the blue dots in Fig. 13(d). Meanwhile, the azimuthally-averaged result of the standard deviation profile predicted by simulation in Section 3.4.1 is also plotted as a black curve in Fig. 13(d). The simulation and experimental results show good agreement. This finding consolidates the efficacy of the simulation model

Optics EXPRESS

in predicting the performance of the metrology system and guiding the setup of optimum experimental conditions. Noting the slope-dependent measurement precision shown in Fig. 13(d), precisions of better than λ/10 for ≤ 5° in slope and better than λ/6 for ≤ 8° in slope (λ = 1318 nm) were achieved with the SS-OCT metrology system. The main reason for the precision degradation with slope has been detailed in Section 3.3. In short, with an increase in the measured slope, the SNR deteriorates as a result of the drop in the collected energy with the increasingly oblique back-reflected light cone. This is essentially an issue common to current optical metrology techniques and thus poses the challenge for noncontact metrology of freeform surfaces. Another contributing factor to the precision degradation with slope is the increasingly tight tolerance of the lateral coordinate errors associated with the measurement point.

4.3 Alvarez freeform surface

The SS-OCT metrology system was then used to measure the Alvarez freeform surface [48] introduced in Section 3.4.2 to assess the system capability in measuring high sag departures and associated slopes of a freeform surface. Figure 14(c) shows a photograph of the Germanium Alvarez surface, which was fabricated through freeform diamond micro-milling [49].

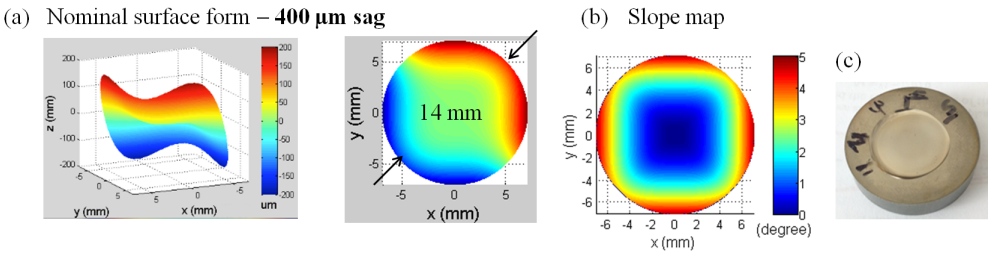

Fig. 14. (a) Two snapshots of the 3D views of an Alvarez freeform surface with a surface sag of ~400 μm PV. (b) The slope map of the Alvarez surface computed from its nominal equation. (c) A photograph of the Alvarez surface with clocking marks on the edge.

Computed from the nominal equation (see Eq. (22)), two snapshots of the 3D views of the Alvarez surface are shown in Fig. 14(a). The theoretical slope profile was also mapped out in Fig. 14(b) by calculating the magnitude of the gradient of the cubic function. The surface sag across the clear aperture is 400 μm PV and the maximum slope is 5°, which exceeds the measurable dynamic range of a conventional commercial laser Fizeau interferometer as the interference fringes become unresolvable. The Zernike fit of the nominal surface with the first 16 terms of the FRINGE Zernike polynomials shows that the surface contains purely three FRINGE Zernike terms, i.e., tilt, coma and trefoil, the magnitudes of which are listed in Table 2. The Zernike fitting coefficients of a typical SS-OCT measured surface figure (see Fig. 15(a) for the corresponding residual profile) is also shown in Table 2.

Figure 15(a) shows a residual profile across the 14 mm clear aperture after the SS-OCT measurement was registered with the nominal surface figure. The residual profile has an RMS of 128 nm, and notably reveals unexpected grating patterns on the test part reminiscent of mid spatial frequencies (MSF) [50,51]. The fast and slow scanning axes are denoted on the plot. A second measurement was conducted with the fast and slow scanning being switched. The corresponding residual profile is shown in Fig. 15(b) with an RMS of 129 nm; however, the grating structure is far less evident from the measurement, indicating there is an interaction of the structure with the scanning pattern. We may then refer to these measured structures as MSF-like structures as it is shown that the scanning directions play a role in profiling these MSFs depending on their orientation. Five measurements were repeated using each scanning scheme, and the standard deviation profile of all 10 measurements is shown in Fig. 15(c), which is on average 93 nm over the clear aperture. This mean precision evaluated across the

Optics EXPRESS

10 experimental measurements is higher than being predicted by simulation in Section 3.4.2, largely due to the measured profile of the MSF-like structures being scanning direction dependent.

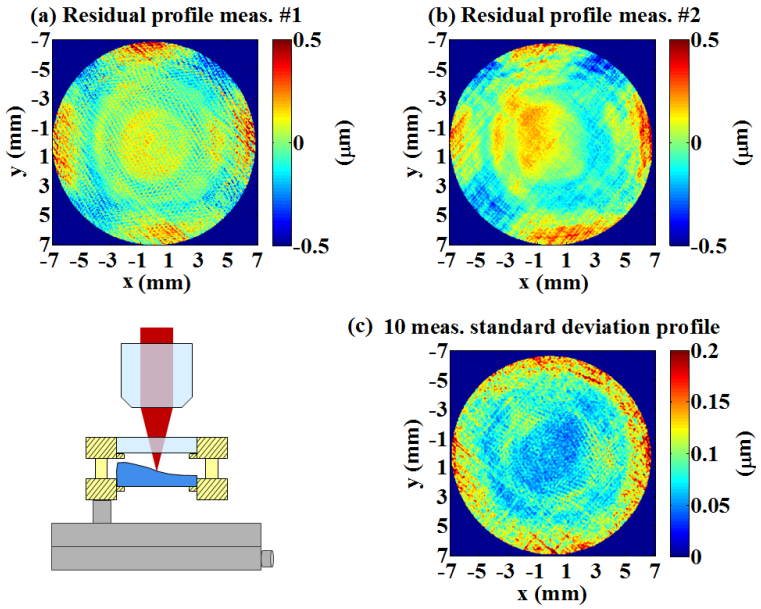

Fig. 15. (a) and (b) are two SS-OCT measurements of the residual profiles of the Alvarez surface after subtracting out its nominal form. (a) and (b) were acquired with a reverse in the orthogonal fast and slow scanning axes. (c) The standard deviation profile across 10 SS-OCT measurements of the Alvarez surface.

To validate the SS-OCT measurements, the same Alvarez surface was also tested by a commercial, precision, low-force tactile profilometer (UA3P, Panasonic Corporation) over a reduced aperture of 12 mm in diameter. Two point cloud measurements on a non-uniform grid were conducted with the fast scanning in the y and x directions, respectively. The fast and slow scanning axes have a scan spacing of 100 μm and 620 μm, respectively. The residual profiles from the two measurements are shown in Figs. 16(a) and 16(b), respectively, with a respective RMS residual of 115 and 122 nm across a 12 mm aperture. The different appearances of the two residual profiles is a result of the fine grating structure beating against the measurement grid in the x and y directions; pattern aliasing occurs if the sampling resolution of the measurement grid is insufficient.

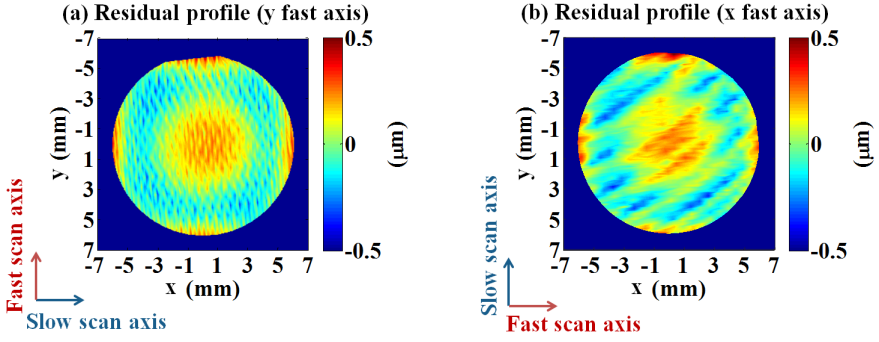

Fig. 16. (a) and (b) are two measured residual profiles of the Alvarez surface by a precision tactile commercial profilometer. (a) and (b) were acquired with a reverse in the fast and slow scanning axes.

Optics EXPRESS

Comparing against the commercial profilometer results, the SS-OCT measurements show good agreement in terms of the residual form error, which indicates the error denotes figure error in the test part. The high resolution measurements obtained from the SS-OCT allowed the observation of residual MSF defects created by the manufacturing tool. These types of defects were much alleviated after subsequent iterations of the manufacturing process with reduced milling step-over.

Table 2. Zernike fitting coefficients of the Alvarez surface profile: nominal form vs. SS-OCT measurements

Zernike surface type	Fringe Zernike fitting coefficient	Nominal equation (μm)	SS-OCT measurement (μm)
Tilt	Z2	97.069	97.067
	Z3	97.069	97.070
Power	Z4	0	–0.011
Primary astigmatism	Z5	0	0.019
	Z6	0	0.041
Primary coma	Z7	48.535	48.540
	Z8	48.535	48.539
Primary spherical	Z9	0	0.080
Trefoil	Z10	48.535	48.554
	Z11	–48.535	–48.532
Secondary astigmatism	Z12	0	–0.007
	Z13	0	–0.003
Secondary coma	Z14	0	–0.034
	Z15	0	0.010
Secondary spherical	Z16	0	–0.012

5. Conclusion

In this work, we demonstrated the development of a point-cloud metrology method based on SS-OCT for the noncontact, high resolution, high accuracy testing of freeform surfaces in the 1 inch diameter class and up to 10° in slope. A common-path setup and rigorous lateral scanning field calibration mitigated scan-induced errors and led to robust system instrumentation.

Furthermore, we proposed and developed a comprehensive model that incorporates the simulation of vertical displacement sensitivity and lateral scanning noise to estimate the system precision in measuring any freeform surfaces. The capability to predict performance

Optics EXPRESS

allows us to select the optimum experimental conditions to achieve the best measurement precision.

In addition, surface reconstruction, rendering and fitting algorithms were developed to evaluate the metrology results and investigate the uncertainty in the measurements. The results of measuring an Alvarez freeform surface with 400-μm PV sag show 93 nm (< λ/14) precision and 128 nm (< λ/10) RMS residual from the nominal shape. The high resolution measurements obtained from the SS-OCT system revealed residual MSFs.

In a broader sense, the theoretical foundations we established to investigate the SNR dependency on surface slope carries particular importance for the freeform-metrology community in general. The methodology we developed to dissect a system and model the SNR fall-off factors may be applied broadly to systematically investigate the performance of various optical and photonics metrological instruments. The current techniques presented in this paper are applicable to the metrology of a broad range of uncoated or coated finished pieces made of glass, polymeric materials, and even metals given the low power of the laser used yielding a focal intensity on the order of only 10^3 W/cm^2, a regime there is no plasma induced laser-metal interaction. Besides the NIR wavelength that the current system operates at, the methods and techniques can be further tailored to different wavelengths such as visible or IR.

The freeform design space has been advanced towards a direction of < 2 mm in surface sag and < 15° in slope. A detailed analysis of recent freeform designs within our group [2,5,6], including spectrometers and head-worn displays, all fall into this category. The current SS-OCT metrology system used to benchmark is limited to 10° in slope, where the precision degrades albeit may be mitigated in part by averaging multiple measurements. Note that the current laser power probing the sample is only ~3 mW, where only specular reflections need to be considered since scattering signals are weak. The ability to keep the uncertainty low at significant slopes may require higher power laser to enhance the system SNR, which in turn brings out the topic of leveraging scattering signals. Future work therefore involves developing a next generation system reconfigured with laser power at least one to two orders of magnitude higher, coupled with a NA > 0.5 objective to precisely probe 15° slopes or possibly higher, as well as utilizing extended depth of focus [52] or refocusing techniques [42] to accommodate 2 mm sags. The efforts will be accompanied by an in-depth investigation of the technology requirement for different levels of surface roughness, to be potentially used for *in situ* metrology. The flexibility of the fiber-based freeform-metrology system we developed may support instrument portability as well as provide an approach to in-line metrology.

Funding

II-VI Foundation; REU fellowship from NSF I/UCRC Center for Freeform Optics IIP-1338877.

Acknowledgments

We thank Profs. Thomas Suleski and Matthew Davies at the University of North Carolina at Charlotte for providing the Alvarez surface. We thank Zygo Corporation for their help with validating the surface profile of an Alvarez freeform surface using a commercial precision profilometer. We thank Di Xu and Jinxin Huang for stimulating discussions about this work. This Research is synergistic with the NSF I/UCRC Center for Freeform Optics (IIP-1338877 and IIP-1338898).